

See discussions, stats, and author profiles for this publication at: <https://www.researchgate.net/publication/235381760>

# Synthesis, Structural Characterization, and Electrical Properties of New Oxygen-Deficient Tetragonal Tungsten Bronzes $\text{Ba}_2\text{NdTi}_{2+x}\text{Nb}_{3-x}\text{O}_{15-x/2}$

ARTICLE in INORGANIC CHEMISTRY · JANUARY 2013

Impact Factor: 4.76 · DOI: 10.1021/ic301156c · Source: PubMed

CITATIONS

10

READS

29

5 AUTHORS, INCLUDING:



Héctor Beltrán

Universitat Jaume I

46 PUBLICATIONS 418 CITATIONS

SEE PROFILE



Eloisa Cordoncillo

Universitat Jaume I

106 PUBLICATIONS 1,351 CITATIONS

SEE PROFILE



A. R. West

The University of Sheffield

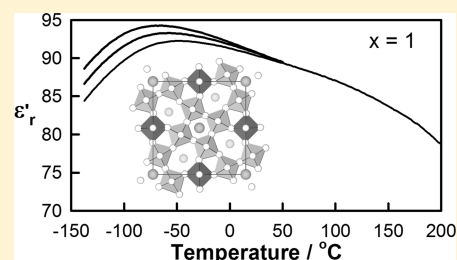
343 PUBLICATIONS 9,485 CITATIONS

SEE PROFILE

## Synthesis, Structural Characterization, and Electrical Properties of New Oxygen-Deficient Tetragonal Tungsten Bronzes

 $\text{Ba}_2\text{NdTi}_{2+x}\text{Nb}_{3-x}\text{O}_{15-x/2}$ Marta Prades,<sup>†</sup> Nahum Masó,<sup>‡</sup> Héctor Beltrán,<sup>†</sup> Eloisa Cordoncillo,<sup>†</sup> and Anthony R. West<sup>\*‡</sup><sup>†</sup>Departamento de Química Inorgánica y Orgánica, Universitat Jaume I, Avda. Sos Baynat s/n, 12071 Castellón, Spain<sup>‡</sup>Department of Materials Science and Engineering, The University of Sheffield, Mappin Street, Sheffield, S1 3JD, U.K.

**ABSTRACT:** Oxygen-deficient tetragonal tungsten bronzes ceramics with general formula  $\text{Ba}_2\text{NdTi}_{2+x}\text{Nb}_{3-x}\text{O}_{15-x/2}$  ( $0 \leq x \leq 1$ ) have been prepared by low temperature solvothermal synthesis with final firing of ceramics at 1100–1300 °C in air. Rietveld refinement of X-ray powder diffraction (XRD) and neutron powder diffraction (ND) data at room temperature of  $\text{Ba}_2\text{NdTi}_3\text{Nb}_2\text{O}_{14.5}$  shows that Ba and Nd are ordered on the 15-coordinate and 12-coordinate sites, respectively, Ti and Nb are disordered nonrandomly over the two octahedral sites, and oxygen vacancies locate preferentially in the coordination sphere of Nd and Ti/Nb(2) atoms. Variable frequency impedance measurements show that samples are poor electronic conductors with activation energies  $\sim 0.8$ – $1.7$  eV, conductivities  $\sim 1 \times 10^{-5} \text{ S cm}^{-1}$  at  $\sim 725$  °C and with some evidence of oxide ion conduction at high  $x$  values. Composition dependence of the dielectric properties shows a transition from classic ferroelectric behavior with  $\text{Ba}_2\text{NdTi}_2\text{Nb}_3\text{O}_{15}$  to a relaxor-like behavior with  $\text{Ba}_2\text{NdTi}_3\text{Nb}_2\text{O}_{14.5}$ . At intermediate compositions, both a first-order phase transition and relaxor-like behavior are observed.



## INTRODUCTION

The tetragonal tungsten bronze (TTB) structure, general formula  $\text{A}_2\text{A}'\text{C}_2\text{BB}'_4\text{O}_{15}$ , can be regarded as a network of corner-sharing ( $\text{BB}'$ ) $\text{O}_6$  octahedra with three types of interstitial sites (A, A', and C) and is obtained from the perovskite structure ( $\text{ABO}_3$ ) by rotation of the  $\text{BO}_6$  octahedra,<sup>1,2</sup> as shown in Figure 1. The chemical composition of TTB oxides is rather flexible since crystallographically nonequivalent cationic A-, A'-, and C-sites can be fully-, or partially occupied or empty, for example,  $\text{K}_3\text{Li}_2\text{Nb}_5\text{O}_{15}$  (all cationic sites full),  $\text{K}_3\text{NiNb}_5\text{O}_{15}$  (C site half occupied),  $\text{Ba}_2\text{NaNb}_5\text{O}_{15}$  (C site empty), and  $\text{BaBiNb}_5\text{O}_{15}$  (A' and C sites empty). The crystallographically distinct octahedral sites, B and B', may be occupied by the same or different cations. An extra degree of freedom for manipulation of the chemical composition is by creation of oxygen vacancies via doping<sup>3,4</sup> and/or atmospheric reduction.<sup>5–7</sup>

A family of TTB-structured phases of general formula  $\text{Ba}_2\text{RETi}_2\text{Nb}_3\text{O}_{15}$  has been reported which includes the larger rare earth, RE, ions ranging from La to Dy and also Bi.<sup>8–16</sup> In these, Ba and RE appear to be fully ordered over the A, A' sites and there is a nonrandom distribution of Ti and Nb over B, B' sites. The La and Bi members show relaxor behavior and the temperature of the permittivity maximum increases with frequency from 185 K at 100 Hz to 300 K at 1 GHz. As the size of the RE cation decreases, two effects are seen: first, the transition temperature increases and reaches 590 K for RE = Gd; second, the nature of the phase transition changes from relaxor to classic first order. Although room temperature X-ray powder diffraction patterns of all the compounds can be indexed on a prototype  $P4/mbm$  or  $P4bm$  space group, electron microscopy studies have revealed deviations from the ideal

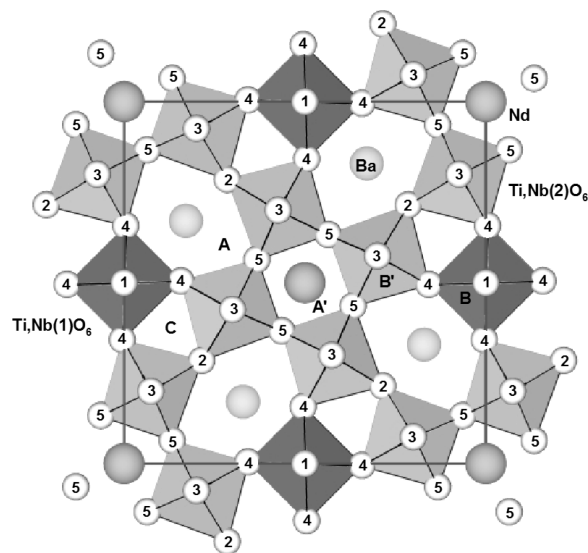


**Figure 1.** Projection of the unit cell of  $\text{Ba}_2\text{NdTi}_3\text{Nb}_2\text{O}_{14.5}$  along [001].  $\text{Ti,Nb(1)O}_6$  and  $\text{Ti,Nb(2)O}_6$  octahedra are shown in black and gray, respectively. Oxygen sites 1 to 5 and cation sites A, A', B, B', and C are indicated.

TTB symmetry caused by two distinct types of two-dimensional structural modulation: Bi- and La-based compounds exhibit a reversible incommensurate (IC)  $\xleftrightarrow{473\text{K}}$   $P4/mbm$  phase transition

Received: May 31, 2012

Published: January 29, 2013

whereas the Nd-, Sm-, and Gd-based phases exhibit reversible  $Im\ a2 \xleftrightarrow{400K} IC \xleftrightarrow{820K} P4/mbm$  phase transitions.<sup>13,16</sup> In addition, the onset of the  $Ima2 \leftrightarrow IC$  transition in  $Ba_2La_{1-x}Nd_xTi_2Nb_3O_{15}$  ceramics was correlated with the size of the cations in the square tunnels ( $A'$  sites), as suggested by the transition temperature, which decreased with increasing substitution of larger La for smaller Nd.<sup>13</sup> The commensurate approximant space group of the IC phase is  $Ama2$  with an orthorhombic supercell  $a \approx 2\sqrt{2}a_{TTB}$ ,  $b \approx \sqrt{2}a_{TTB}$ ,  $c \approx 2a_{TTB}$  whereas the orthorhombic  $Ima2$  supercell lattice parameters are  $a \approx b \approx \sqrt{2}a_{TTB}$  and  $c \approx 2c_{TTB}$ .  $Ba_2NdTi_2Nb_3O_{15}$  also shows two further dielectric relaxations over the temperature range 200–350 K, which have been linked to structural fluctuations associated with coupling between the polarizability in the  $ab$  plane of the unit cell and the  $c$  axis displacement and random field effects.<sup>17</sup>

Usually, the synthesis of these TTB phases is achieved by high temperature solid state reaction, requiring prolonged heat treatments. Recently, the Sm and Nd analogues have been synthesized using a low temperature solvothermal route, and their permittivity vs temperature data exhibit two unusual features as ferroelectric materials:<sup>18</sup> first, a significant hysteresis between heating and cooling cycles in their phase transition behavior and second, a huge depression in the Curie–Weiss temperature  $T_0$ , which is very different from the behavior usually observed in first order ferroelectrics.

We report here the crystal structure and electrical properties of a new family of oxygen-deficient TTB ceramics with general formula  $Ba_2NdTi_{2+x}Nb_{3-x}O_{15-x/2}$  obtained by varying the Ti/Nb ratio.

## EXPERIMENTAL SECTION

Samples with compositions based on the formula  $Ba_2NdTi_{2+x}Nb_{3-x}O_{15-x/2}$  ( $0 \leq x \leq 3$ ) were prepared by a solvothermal process using  $Ba(CH_3COO)_2$ : 99%,  $Nd(C_3H_7O)_3$ : 99.9%,  $Ti(C_3H_7O)_4$ : 98%, and  $Nb(OC_2H_5)_5$ : >99.9%, all Strem Chemicals, as described in ref 18.

The solvothermal-derived powder samples were gradually heated to temperatures in the range 1100–1300 °C for 2 h, pressed into pellets and sintered in air at the same maximum temperature for 2 h after which, pellets were slow-cooled inside the furnace. Pellet densities were ~75 and ~85% at 1100 and 1300 °C, respectively. Product phases were identified by X-ray powder diffraction (XRD) using a Bruker D4 Endeavor diffractometer,  $CuK\alpha$  radiation. The lattice parameters were determined by least-squares refinement for reflections in the range  $10^\circ < 2\theta < 70^\circ$ , using the software WinXPow version 1.06.

Scanning electron micrographs (SEMs) of pellet surfaces were taken on a SEM Leica, Leo 440 model, equipped with a spectrometer for energy dispersion of X-rays (EDX), using the following operation parameters: acceleration voltage 20 kV, measuring time 100 s, working distance 25 mm, counting rate 1.2 kcps. The samples were fixed on Al holders and coated with graphite.

Structural characterization of  $Ba_2NdTi_3Nb_2O_{14.5}$  ( $x = 1$ ) powder was carried out by Rietveld refinement of X-ray and neutron powder diffraction (ND) data obtained at room temperature. XRD data were collected using a Stoe StadiP diffractometer,  $CuK\alpha$  radiation (wavelength 1.54056 Å) with a small, linear position-sensitive detector; ND data were collected at the Institut Laue-Langevin, Grenoble, France, on the D2B diffractometer (wavelength 1.594 Å). Combined refinement of XRD and ND data sets was carried out using GSAS+EXPGUI software.<sup>19</sup> The errors quoted are as given by GSAS.

For electrical property measurements, electrodes were fabricated on opposite pellet faces from Pt paste, which was dried and decomposed by gradually heating to 900 °C. Samples with electrodes attached were placed into a conductivity jig and electrical property data recorded using a combination of an Agilent 4294A and Alpha–N Novocontrol impedance analyzers over the frequency range 10 mHz (Novocontrol) or 40 Hz (Agilent) to 13 MHz and over the temperature range,

–150 to 900 °C. Impedance data were corrected for overall pellet geometry and for the blank cell capacitance (“jig correction”).

## RESULTS

Samples of  $Ba_2NdTi_{2+x}Nb_{3-x}O_{15-x/2}$  over the composition range  $0 \leq x \leq 1$  were single phase by XRD after firing at 1100 and 1300 °C whereas those for  $x \geq 1.5$  contained secondary phase(s). The patterns were indexed accordingly with refined lattice parameters summarized in Figure 2. These show a

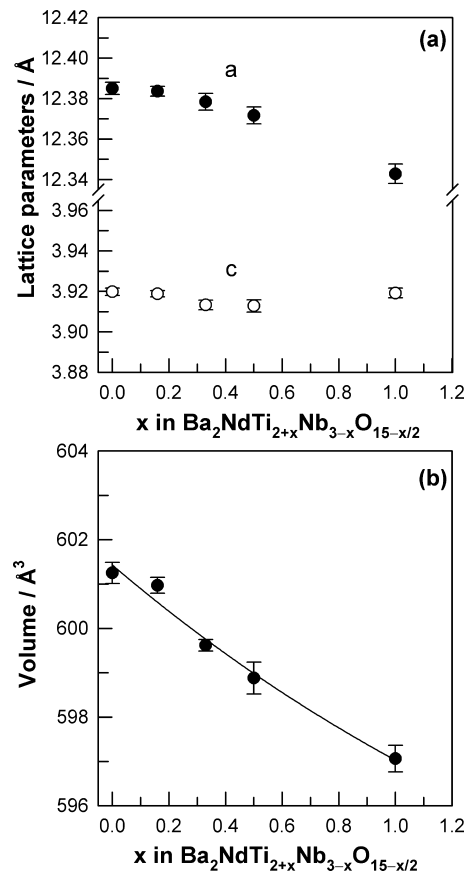


**Figure 2.** Lattice parameters (a) and cell volume (b) of the  $Ba_2NdTi_{2+x}Nb_{3-x}O_{15-x/2}$  solid solution. Error bars represent  $2\sigma$ . Solid line in (b) is to guide the eye.

decrease of  $a$  and  $V$  with  $x$  whereas  $c$  remains constant. These data are consistent with the smaller size of Ti (74.5 pm) compared to that of Nb (78 pm). There was also no evidence for the presence of any secondary phases in compositions  $0 \leq x \leq 1$  by backscattered electron analysis and EDX. A SEM image of the pellet surface of  $Ba_2NdTi_3Nb_2O_{14.5}$ ,  $x = 1$ , sintered at 1300 °C is shown in Figure 3. It is concluded, therefore, that a solid solution forms over the composition range  $0 \leq x \leq 1$ .

The crystal structure of the La analogue of composition  $x = 0$ ,  $Ba_2LaTi_2Nb_3O_{15}$ , has been studied previously using ND data<sup>12</sup> and preliminary results obtained on  $Ba_2NdTi_2Nb_3O_{15}$  (unpublished). Here we report the structure of the  $x = 1$  composition  $Ba_2NdTi_3Nb_2O_{14.5}$  which had the specific objectives of locating the oxygen vacancies and determining the Ti/Nb site distribution. Both XRD and ND data obtained at room temperature were indexed and refined on a tetragonal unit cell with lattice parameters  $a \sim 12.344$  Å,  $c \sim 3.916$  Å and space group  $P4/mbm$ . There was no evidence of extra-reflections in the

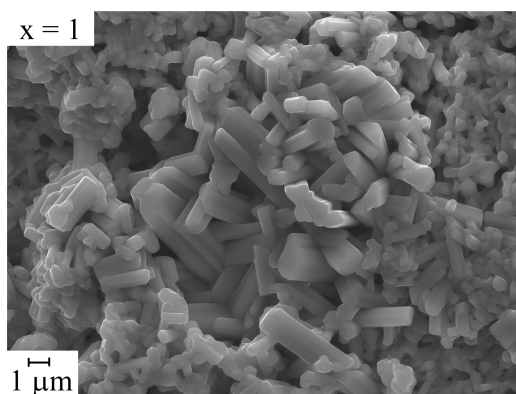


**Figure 3.** SEM of the surface of a pellet of  $\text{Ba}_2\text{NdTi}_3\text{Nb}_2\text{O}_{14.5}$  sintered at 1300 °C.

XRD and ND patterns that could indicate an orthorhombic supercell; this is not the case for  $x = 0$ , however, which shows some weak extra reflections in the ND pattern (Figure 4), but

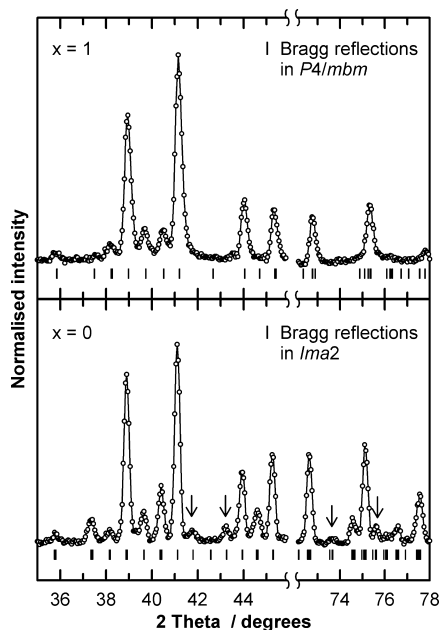


**Figure 4.** ND patterns of  $\text{Ba}_2\text{NdTi}_{2+x}\text{Nb}_{3-x}\text{O}_{15-x/2}$  ceramics. Arrows show some weak reflections which indicate an orthorhombic unit cell with lattice parameters  $a \approx b \approx \sqrt{2}a_{\text{TTB}}$ ,  $c \approx 2c_{\text{TTB}}$  and space group  $\text{Ima}2$ .

not in the XRD pattern; these can be indexed and refined on a larger orthorhombic unit cell<sup>13,16</sup> with  $a \approx b \approx \sqrt{2}a_{\text{TTB}} \approx 17.5$  Å,  $c \approx 2c_{\text{TTB}} \approx 7.85$  Å and space group  $\text{Ima}2$ . Work is in progress to refine the structure of  $\text{Ba}_2\text{NdTi}_2\text{Nb}_3\text{O}_{15}$  ( $x = 0$ ) and especially, determine the nature of the supercell structure. For the present paper, we note that the crystal structure of  $\text{Ba}_2\text{NdTi}_3\text{Nb}_2\text{O}_{14.5}$  ( $x = 1$ ) is macroscopically tetragonal by both XRD and ND.

To generate a starting model for  $\text{Ba}_2\text{NdTi}_3\text{Nb}_2\text{O}_{14.5}$ ,  $x = 1$ , the data of Kirk et al.<sup>9</sup> for  $\text{Ba}_2\text{LaTi}_2\text{Nb}_3\text{O}_{15}$ ,  $x = 0$ , (space group  $P4/mbm$ ) were used. Ba and Nd were placed on the positions 4g (15-coordinate site) and 2a (12-coordinate site), respectively, whereas Ti and Nb were distributed statistically on the octahedral sites (positions 2c and 8j corresponding to Ti,Nb(1) and Ti,Nb(2), respectively). At this stage, oxygen occupancies

were set to be full. The refinement converged fully and was good for both XRD and ND data sets (not shown). Inspection of the  $U_{\text{iso}}$  values showed, however, somewhat large values for O(1,3,5) and Ti/Nb(1) and a slightly negative value for Ti/Nb(2). This indicated that Ti and Nb might not be distributed statistically over the two sets of sites with instead, a slight preference of Nb for site (8j) and Ti for site (2c). In a previous study using ND data of  $\text{Ba}_2\text{LaTi}_2\text{Nb}_3\text{O}_{15}$  (ref 12), the Ti/Nb distribution was also found to be nonstatistical with  $\sim 0.465/0.535$  (2c) and  $\sim 0.385/0.615$  (8j) occupancy ratios. Preliminary analysis of ND data for  $\text{Ba}_2\text{NdTi}_2\text{Nb}_3\text{O}_{15}$ ,  $x = 0$ , (unpublished) confirmed the nonrandom nature of the Ti/Nb site distribution.

Different amounts of cross-substitution were next introduced into the refinements to determine their effect on the  $U_{\text{iso}}$  values,  $\chi^2$  and R factors, as summarized in Figure 5. On increasing

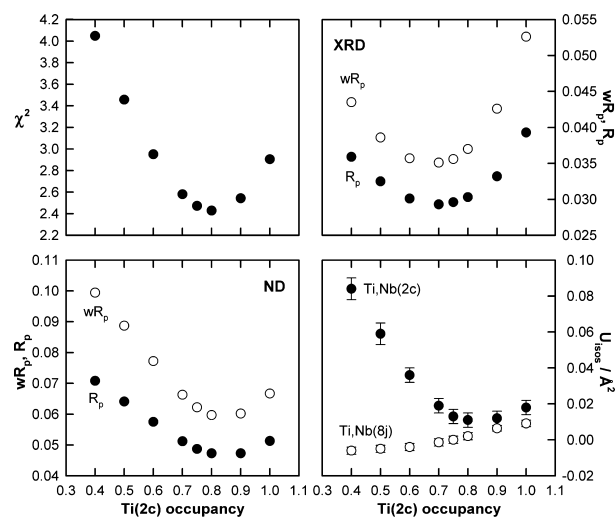


**Figure 5.**  $\chi^2$  (XRD+ND),  $wR_p$ ,  $R_p$  (background subtracted) and isotropic temperature factors ( $U_{\text{iso}}$ ) of Ti,Nb(2c,8j) for different amounts of cross-substitution.

Ti(2c) occupancy,  $\chi^2$ , R factors, and the  $U_{\text{iso}}$  value of site Ti,Nb(2c) passed through a minimum at 0.7–0.85 whereas  $U_{\text{iso}}$  for Ti,Nb(8j) increased to slightly positive values; the  $U_{\text{iso}}$  values of Ba(1), Nd(1), O(1), O(2), O(3), O(4), and O(5) remained approximately constant at 0.0265(25), 0.0145(15), 0.0415(25), 0.0075(15), 0.0555(35), 0.0195(35), and 0.0395(25) Å<sup>2</sup>, respectively. It was, therefore, concluded that Ti/Nb were disordered over the B, B' octahedral sites with a preference of Ti for site (2c), but the estimated occupancy ratio depended on which statistical parameter ( $\chi^2$ ,  $wR_p$  or  $R_p$ ) was used to evaluate the goodness of fit. Using  $\chi^2$  as a reference statistical parameter, the occupancies of Ti(1) and Ti(2) sites were set at  $\sim 0.8$  and  $\sim 0.55$ , respectively.

The occupancies of Ti(1), Nb(1), Ti(2), Nb(2), O(2), and O(4) were therefore fixed to 0.80, 0.20, 0.55, 0.45, 1 and 1, respectively. The large  $U_{\text{iso}}$  values of O(1,3,5) might indicate a lower occupancy on these sites; different amounts of O(1,3,5) occupancy introduced into the refinements to determine the effect on the  $U_{\text{iso}}$  values,  $\chi^2$ , and R factors.  $\chi^2$  and R factors improved somewhat (not shown) on distributing the oxygen vacancies over O(1,3,5) but worsened on confining the oxygen vacancies to either O(1), O(3), or O(5), especially for O(1). The occupancies of O(1,3,5) were therefore refined independently. Final parameters, selected bond distances and angles, and refinement profiles are summarized in Tables 1 and 2 and



**Table 1.** Lattice Parameters, Atomic Positions, And Isotropic Temperature Factors for Ba<sub>2</sub>NdTi<sub>3</sub>Nb<sub>2</sub>O<sub>14.5</sub> at Room Temperature<sup>a,b,c</sup>

atom	site	x	y	z	site occupancy	U <sub>iso</sub> (Å <sup>2</sup> )
Nd(1)	2a	0	0	0	1	0.0146(8)
Ba(1)	4g	0.1709(1)	0.6709(1)	0	1	0.0264(9)
Ti(1)	2c	0	0.5	0.5	0.8	0.0116(18)
Nb(1)	2c	0	0.5	0.5	0.2	0.0116(18)
Ti(2)	8j	0.0745(2)	0.2144(2)	0.5	0.55	0.0025(9)
Nb(2)	8j	0.0745(2)	0.2144(2)	0.5	0.45	0.0025(9)
O(1)	2d	0	0.5	0	0.95(2)	0.039(3)
O(2)	4h	0.2852(2)	0.7852(2)	0.5	1	0.0100(10)
O(3)	8i	0.07410(50)	0.2002(4)	0	0.96(1)	0.055(2)
O(4)	8j	0.3426(3)	0.0046(3)	0.5	1	0.025(1)
O(5)	8j	0.13306(39)	0.0641(4)	0.5	0.93(1)	0.036(1)

<sup>a</sup>Space group *P4/mbm* (No. 127). <sup>b</sup>*a* = *b* = 12.3437(2) Å, *c* = 3.9155(1) Å, and *V* = 596.600(30) Å<sup>3</sup>. <sup>c</sup> $\chi^2$  (XRD+ND) = 2.415 for 74 variables. XRD:  $\chi^2$  = 1.944; *wR<sub>p</sub>* = 0.0360 and *R<sub>p</sub>* = 0.0295 (background subtracted). ND:  $\chi^2$  = 2.710; *wR<sub>p</sub>* = 0.0596 and *R<sub>p</sub>* = 0.0470 (background subtracted).

**Table 2.** Bond Lengths for Ba<sub>2</sub>NdTi<sub>3</sub>Nb<sub>2</sub>O<sub>14.5</sub> at Room Temperature

bond lengths (Å)			bond angles (degrees)	
Ba–O(1)	2.983(2)		O(1)–Ti,Nb(1)–O(1)	180
Ba–O(2)	2.795(4)	×2	O(1)–Ti,Nb(1)–O(4)	90
Ba–O(3)	3.169(6)	×2	O(4)–Ti,Nb(1)–O(4)	180
	3.417(6)	×2		93.4(2)
Ba–O(4)	2.8413(30)	×4		86.6(2)
Ba–O(5)	3.3810(40)	×4	O(2)–Ti,Nb(2)–O(3)	92.4(2)
Nd–O(3)	2.635(5)	×4	O(2)–Ti,Nb(2)–O(4)	94.9(2)
Nd–O(5)	2.675(3)	×8	O(2)–Ti,Nb(2)–O(5)	95.5(2)
Ti,Nb(1)–O(1)	1.95777(4)	×2		176.3 (2)
Ti,Nb(1)–O(4)	1.944(4)	×4	O(3)–Ti,Nb(2)–O(3)	169.8(3)
Ti,Nb(2)–O(2)	1.9400(30)		O(3)–Ti,Nb(2)–O(4)	94.3(2)
Ti,Nb(2)–O(3)	1.9656(5)	×2	O(3)–Ti,Nb(2)–O(5)	85.3(2)
Ti,Nb(2)–O(4)	1.859(4)			87.3(2)
Ti,Nb(2)–O(5)	1.992(6)		O(4)–Ti,Nb(2)–O(5)	169.6(2)
Ti,Nb(2)–O(5)	1.983(6)			88.7(2)
			O(5)–Ti,Nb(2)–O(5)	80.8(3)

Figure 6. On considering the occupancy and multiplicity of each oxygen site, the distribution of oxygen vacancies was ~10(4), ~32(8), and ~56(8) % for O(1), O(3), and O(5), respectively. Thus, oxygen vacancies were located preferentially in the coordination spheres of Nd and Ti/Nb(2), Table 2, and Figure 1.

Finally, the possibility of cross-substitution of Ba and Nd over the 15- and 12-coordinate sites was tested. On increasing the Ba occupancy on the 12-coordinate site (2a),  $\chi^2$  and *R* factors worsened, which confirmed that Ba and Nd atoms are ordered over the 15-coordinate (A) and 12-coordinate (A') sites, respectively.

Electrical properties of Ba<sub>2</sub>NdTi<sub>2+x</sub>Nb<sub>3-x</sub>O<sub>15-x/2</sub> ceramics were measured by impedance spectroscopy using pellets fired at 1100 and 1300 °C in air. A selection of typical results is shown in Figure 7 for *x* = 0.66. A similar response was seen for all compositions. Generally, impedance complex plane plots, Figure 7a, showed an asymmetric arc with a distortion from ideal semicircular shape at low frequencies; the distortion was seen most clearly for composition *x* = 1.0. *Z''*/*M''* spectroscopic plots, Figure 7b, showed a single peak in each spectrum with approximately similar peak maximum frequencies but an additional low frequency shoulder in the *Z''* spectrum associated with the low frequency distortion in the *Z''* vs *Z'* plots. Since *M''* spectra are dominated by low capacitance bulk effects, the data in Figure 7b indicate that the main resistive component of

the sample (the *Z''* peak), is associated with the sample bulk (*M''* peak).

Capacitance (*C'*) spectroscopic plots, Figure 7c, showed a frequency-independent, but temperature-dependent plateau at high frequencies, for example, ~5 × 10<sup>-12</sup> F cm<sup>-1</sup> at 628 °C, attributed to the sample bulk; a second, poorly resolved plateau at intermediate frequency with capacitance ~ (1 to 10) × 10<sup>-10</sup> F cm<sup>-1</sup> is attributed to a conventional grain boundary and correlates with the shoulder peak seen in *Z''*; at low frequency, *C'* increased further to values ~10<sup>-9</sup> to 10<sup>-6</sup> F cm<sup>-1</sup>, depending on composition and temperature. In addition, the beginnings of a separate low frequency arc is seen in the impedance complex plane plots, especially for *x* = 1 when measured at high temperatures and in an atmosphere of N<sub>2</sub>, Figure 8. This effect, and the high capacitance values, is taken to indicate the occurrence of some oxide ion conduction.

The total sample resistance was obtained from the low frequency intercept of the main arc on the *Z'* axis of the impedance complex plane plots and is shown in Arrhenius format in Figure 9 for samples sintered at 1100 °C. All plots show curvature with increased activation energy at high temperatures. Similar shaped curved plots were obtained at the two sintering temperatures but the conductivity increased by a factor of 2 to 3 on sintering at 1300 °C, possibly as a consequence of the increased pellet densities. In addition, the conductivities

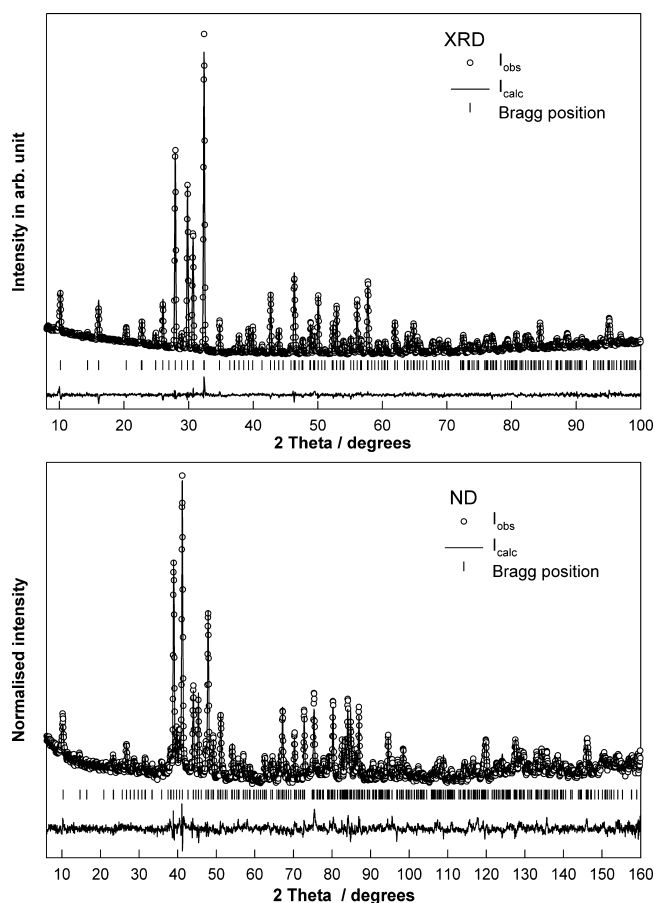


**Figure 6.** Experimental, calculated, and difference XRD and ND patterns for  $\text{Ba}_2\text{NdTi}_3\text{Nb}_2\text{O}_{14.5}$  at room temperature.

showed a gradual increase with  $x$ , with a difference of up to 1 order of magnitude between  $x = 0$  and  $x = 1$ . Although the Arrhenius plots were curved for most, or all, of the temperature ranges over which data were obtained, the limiting activation energies at low and high temperatures were  $\sim 0.8$  and  $\sim 1.7$  eV, respectively.

Further insight into the conduction mechanisms was obtained from impedance measurements made in different atmospheres, Figure 8. Measurements were made at constant temperature, but the atmosphere ( $\text{O}_2$ , air and  $\text{N}_2$ ) was varied during measurement. As the measuring atmosphere changed from  $\text{N}_2$  to air to  $\text{O}_2$ , the sample resistance increased for  $x = 0$  whereas it decreased for compositions with  $x > 0$ . Since, with increasing oxygen partial pressure, electrons are withdrawn from the sample according to reaction:  $\text{O}_2 + \text{V}_{\text{O}}^{\bullet\bullet} + 4\text{e}^- \rightarrow 2\text{O}_{\text{O}}^{\times}$ , the conduction mechanism is  $n$ -type for  $x = 0$  but  $p$ -type for  $x > 0$ .

Fixed frequency relative permittivity data ( $\epsilon'_r$ ) as a function of temperature for four compositions are shown in Figure 10.  $\text{Ba}_2\text{NdTi}_2\text{Nb}_3\text{O}_{15}$  ( $x = 0$ ) showed a maximum permittivity of  $\sim 290$  at  $T_C \sim 166^\circ\text{C}$  and frequency-independent permittivity below  $T_C$  (not shown). On increasing  $x$ ,  $T_C$  decreased linearly, the peak in the  $\epsilon'_r$  vs temperature profile at  $T_C$  gradually vanished, and a rather broad peak with relaxor-like behavior appeared around  $-60^\circ\text{C}$ . Thus, a transition from classic ferroelectric behavior to relaxor-like behavior was observed. This behavior resembles those of  $\text{Ba}_3\text{RETi}_2\text{Nb}_3\text{O}_{15}$  and  $\text{Ba}_2\text{La}_{1-x}\text{Nd}_x\text{Ti}_2\text{Nb}_3\text{O}_{15}$  ceramics on increasing the RE size from Gd to La and increasing La content, respectively.<sup>13,16</sup> The dielectric loss ( $\tan \delta$ ) also exhibited frequency dependence with

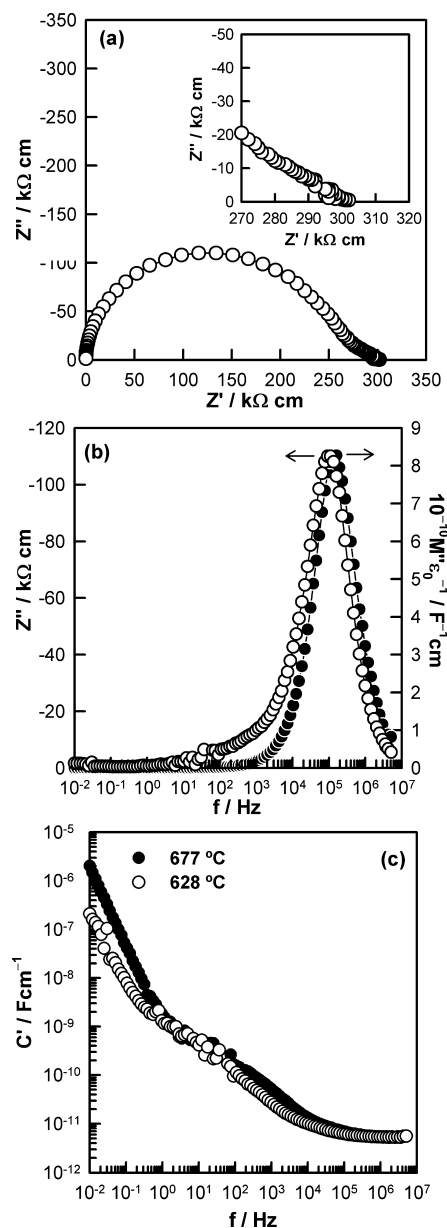


**Figure 7.** (a) Impedance complex plane plot, (b)  $Z''$  and  $M''$  spectroscopic plots, and (c)  $C'$  spectroscopic plot of  $\text{Ba}_2\text{NdTi}_{2.66}\text{Nb}_{2.34}\text{O}_{14.67}$  sintered at  $1100^\circ\text{C}$ . The measurement was made at  $628^\circ\text{C}$  for (a, b) and  $628, 677^\circ\text{C}$  for (c).

values lower than  $\sim 0.025$ . Below room temperature, where relaxor-like behavior in  $\epsilon'_r$  is seen, the loss peak increased in magnitude and shifted to higher temperatures with increasing frequency.

## DISCUSSION

Oxygen-deficient tetragonal tungsten bronzes ceramics with general formula  $\text{Ba}_2\text{NdTi}_{2+x}\text{Nb}_{3-x}\text{O}_{15-x/2}$  form over the composition range  $0 \leq x \leq 1$ . The solid solutions are macroscopically tetragonal or pseudotetragonal with evidence for an orthorhombic supercell for  $x = 0$ . The structure of composition  $x = 1$  has been determined by Rietveld refinement of combined room temperature XRD and ND data. Ba and Nd are fully ordered over A and A' sites; the Ti/Nb distribution over B, B' sites is nonstatistical with a preference of Ti for the 2c, B sites. The overall Ti content increases between  $x = 0$  and  $x = 1$ , and it

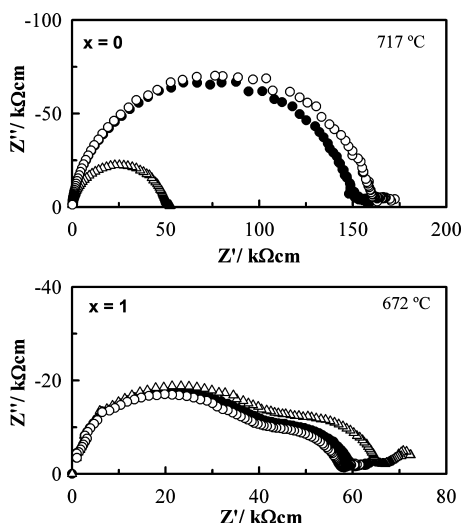


**Figure 8.** Impedance complex plane plots in different measuring atmospheres:  $N_2$  ( $\Delta$ ), air ( $\bullet$ ) and  $O_2$  ( $\circ$ ), for (a)  $Ba_2NdTi_2Nb_3O_{15}$  and (b)  $Ba_2NdTi_3Nb_2O_{14.5}$  ceramics sintered at  $1300^\circ C$ .

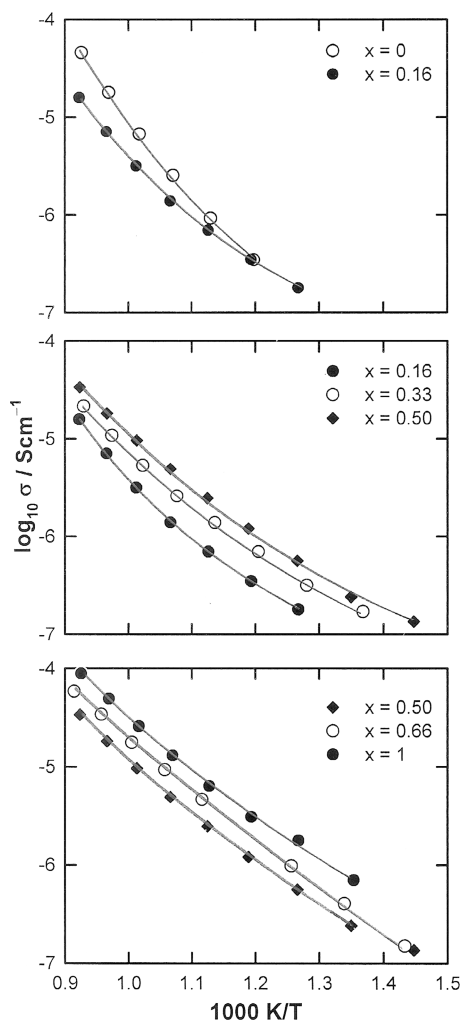


**Figure 9.** Arrhenius plots of total conductivity of  $Ba_2NdTi_{2+x}Nb_{3-x}O_{15-x/2}$  ceramics sintered at  $1100^\circ C$ .

appears that the preference of Ti for the 2c sites may also increase, although full occupancy of the 2c site by Ti is not achieved.

Oxygen vacancies are found preferentially on sites O(3) and O(5) and a much smaller concentration on O(1). These O(3, 5) sites are associated exclusively with the 8j B' sites, Figure 1. The effect of the oxygen vacancies is presumably to reduce the site coordination from 6 to 5; the vacancies may be preferentially associated with the smaller Ti atoms, rather than with Nb, but also because the extra Ti may be regarded as an acceptor dopant when it substitutes for Nb with creation of oxygen vacancies as the charge compensation mechanism. Since each O(3, 5) links two octahedra at their corners, the effect of a vacancy is to create two square pyramids with presumably Ti–Ti repulsions leading to a tendency for Ti cations to be displaced toward the centers of the pyramids. With these various assumptions, it is estimated that  $\sim 40\%$  of the Ti(2) sites have coordination 5 instead of 6 in  $x = 1$ .

Locally, therefore, the crystal structure may have a more distinctive local structure than represented by the average coordinates and occupancies given by the Rietveld refinement results. Although there is no evidence of a supercell in the XRD/ND data, it will be interesting to make further investigations by electron microscopy.

The electrical property data cover two parameters of interest, the permittivity and conductivity. The permittivity data show two main features: a first order, sharp peak for  $x = 0$  which moves to lower temperature and broadens with increasing  $x$ ; a broad, frequency-dependent relaxor peak which gradually dominates the permittivity profile. The permittivity data may be influenced by several structural effects. It is presumed that the ferroelectricity is associated with the B, B' site cations, but there are two crystallographic sites (or possibly more in the supercells) and a distribution of two cations, Ti and Nb, over both sets of sites.

Previously, first order and relaxor transitions in related TTb phases have been attributed to difference in sizes of Ba and rare earth cations occupying A and A' sites. Thus, a similar transition from *classic* ferroelectric behavior to relaxor-like behavior was observed in  $Ba_2RETi_2Nb_3O_{15}$  ( $RE = Bi^{3+}, La^{3+}, Nd^{3+}, Sm^{3+}, Gd^{3+}$ ),<sup>13</sup>  $Ba_2La_{1-x}Nd_xTi_2Nb_3O_{15}$ ,<sup>16</sup>  $(Ba_xSr_{1-x})_2NdTi_2Nb_3O_{15}$ ,<sup>20</sup>  $Sr_2La_xNd_{1-x}Ti_2Nb_3O_{15}$ ,<sup>21</sup>  $Sr_2La_{1-x}Sm_xTi_2Nb_3O_{15}$ <sup>22</sup> ceramics and discussed according to the radius difference on the A, A'-sites between Ba/Sr and RE atoms, which are ordered over the 15- and 12-coordinate sites, respectively. These compounds show a first order phase transition at  $T_C$  and a relaxor-like transition at  $T_m$  for large and small radius difference, respectively; both transitions are seen at intermediate radius difference. The origin of the low temperature relaxor-like behavior of  $Sr_2NaNb_3O_{15}$ , which exhibits a disordered distribution of Sr and Na over the 15- and 12-coordinate sites whereas the B-site is fully occupied by Nb atoms, has been attributed instead to a smeared out phase transition to a frustrated ferroelectric/ferroelastic low temperature state since no structural transition but a change in the elastic properties of the material were observed.<sup>23</sup>

B-site doping effects in relaxor and ferroelectric TTb's such as  $Ba_6M^{3+}Nb_9O_{30}$  and  $Ba_6M^{4+}Nb_8O_{30}$  have been reported by Arnold and Morrison,<sup>24</sup> who have shown that  $T_C$  (or  $T_m$ ) increases linearly with the degree of anisotropy (strain), quantified by the tetragonality (ratio of  $c/a$ ), irrespective of the size or charge associated with the metal on the B-site. Our results in the  $Ba_2NdTi_{2+x}Nb_{3-x}O_{15-x/2}$  solid solution show a slight increase in tetragonality with  $x$  from 0.3165(2) for  $x = 0$  to 0.3175(2) at  $x = 1.0$  while  $T_C$  decreases linearly and  $T_m$  remains

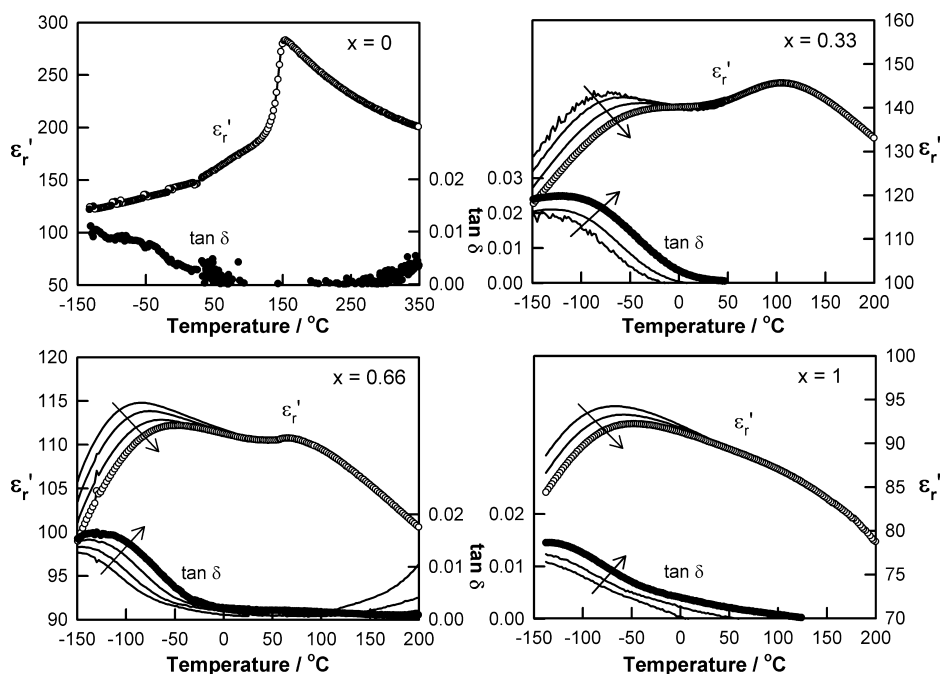


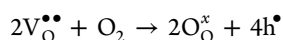
**Figure 10.** Relative permittivity ( $\epsilon_r'$ ) and  $\tan \delta$  data as a function of temperature for several compositions. Arrow indicates the direction of increasing frequency from 1 kHz to 1 MHz. Noisy  $\epsilon_r'$  data and  $\tan \delta$  values below the measuring limit of the analyzer ( $\sim 0.0003$ ) have been omitted.

almost constant. This is therefore not consistent with the strain model.<sup>24</sup>

The present results offer a rather different scenario for the effect of composition and crystal structure on electrical properties. In this, the A,A' site occupancies are unchanged, but there appears to be a change in the nonstatistical occupancy of B,B' sites. Further, oxygen vacancies are present which are associated primarily with O(3,5) and are exclusive to B' site coordination. If it is assumed that the vacancies are primarily associated with Ti, then 40% of the Ti<sub>B'</sub> sites have coordination 5 instead of octahedral. We are not aware of any ferroelectric material in which 5-coordinate Ti forms the polar center and therefore, the transition from first order to relaxor behavior could be associated with the disruptive influence of 5-coordinate Ti on the polar domains of TiO<sub>6</sub> octahedra.

The conductivity data show a complex temperature- and composition-dependence. Measurements in different atmospheres indicate *n*-type behavior for  $x = 0$ , *p*-type behavior for  $x > 0$ , and some evidence for oxide ion conduction, especially at higher values of  $x$ . Nevertheless, the conductivity values are very low, and the materials are good insulators.

The possibility of some oxide ion conduction may be rationalized easily from the solid solution mechanism in which oxygen vacancies are associated with the Ti acceptor dopants. The *p*-type conductivity observed for  $x > 0$  could also be associated with the oxygen vacancies since O<sub>2</sub> from the atmosphere may be absorbed according to



Oxygen absorption leading to *p*-type conductivity is a commonly observed feature of materials that have oxygen vacancies. For absorption and ionization to occur, a source of electrons is needed; this could be impurity cations that can be ionized or O<sup>2-</sup> ions in underbonded environments such as in the vicinity of acceptor dopants that can ionize to O<sup>-</sup> ions.<sup>25–30</sup>

The *n*-type conductivity of composition  $x = 0$  is harder to explain. Possibly the sample contains a trace amount of donor dopants, such as a slight excess of Nd<sup>3+</sup> ions on A sites leading to B, B'-site electron doping. Similar behavior was seen for samples of  $x = 0$  that were either quenched or slow-cooled from high temperatures and therefore, the possibility of a small amount of reversible O<sub>2</sub> loss at high temperatures could not amount for the *n*-type behavior.

Finally, these results point to possible high temperature dielectric applications as Class-II X7R/X8R-type dielectrics where a capacitance tolerance ( $\Delta C'/C'$ ) within  $\pm 15\%$  and  $\tan \delta$  values lower than 0.025 are necessary in the temperature range  $-55\text{ }^{\circ}\text{C}$  to  $+150\text{ }^{\circ}\text{C}$ . Ba<sub>2</sub>NdTi<sub>2+x</sub>Nb<sub>3-x</sub>O<sub>15-x/2</sub> ceramics with  $x \sim 0.33$  show an almost temperature-stable capacitance and low  $\tan \delta$  values over a large temperature range. An alternative approach would be to fabricate a composite of the two end members ( $x = 0$  and 1) to form a heterogeneous microstructure with a flattened temperature dependence, similar to that reported for mixtures of Ba<sub>2</sub>RETi<sub>2</sub>Nb<sub>3</sub>O<sub>15</sub> (RE = La, Nd and Sm).<sup>15</sup>

## CONCLUSIONS

Oxygen-deficient TTBS with general formula Ba<sub>2</sub>NdTi<sub>2+x</sub>Nb<sub>3-x</sub>O<sub>15-x/2</sub> ( $0 \leq x \leq 1$ ) have been prepared by low temperature solvothermal synthesis, and the crystal structure of Ba<sub>2</sub>NdTi<sub>3</sub>Nb<sub>2</sub>O<sub>14.5</sub> ( $x = 1$ ) has been determined by Rietveld refinement of XRD and ND data at room temperature. Ba and Nd are ordered over the 15-coordinate and 12-coordinate sites, respectively, Ti and Nb atoms are disordered, but nonrandomly, over octahedral sites, and oxygen vacancies are distributed over three sets of oxygen sites, O(1) and especially O(3) and O(5). Ba<sub>2</sub>NdTi<sub>2+x</sub>Nb<sub>3-x</sub>O<sub>15-x/2</sub> ceramics are very good insulators with  $\tan \delta < 0.025$  over the temperature range  $-150$  to  $+200\text{ }^{\circ}\text{C}$  and show a transition from *classic* ferroelectric behavior to relaxor-like behavior with  $x$ .



## ■ AUTHOR INFORMATION

## Corresponding Author

\*E-mail: a.r.west@sheffield.ac.uk.

## Notes

The authors declare no competing financial interest.

## ■ ACKNOWLEDGMENTS

We thank The Institut Laue-Langevin, Dr. Emmanuelle Suard and Mr. Ludovic Gendrin (The Institut Laue-Langevin, diffraction group, D2B) for data collection. We thank the EPSRC (N.M., A.R.W.) and “Bancaja-Universitat Jaume I”- project No. P1 1B2011-25 (M.P., H.B., E.C.) for financial support. M.P. thanks Universitat Jaume I for a fellowship (CONT/2011/08). We thank the reviewers for thoughtful comments.

## ■ REFERENCES

- (1) Jamieson, P. B.; Abrahams, S. C.; Bernstein, J. L. *J. Chem. Phys.* **1968**, *48*, 5048.
- (2) Trubelja, M. P.; Ryba, E.; Smith, D. K. *J. Mater. Sci.* **1996**, *31*, 1435.
- (3) Zhang, G.-K.; Ouyang, S.-X.; Fang, L.; Qin, L.-Q.; Zhang, Q. *J. Wuhan Univ. Technol.* **2001**, *16*, 30.
- (4) Vanderah, T. A.; Collins, T. R.; Wong-Ng, W.; Roth, R. S.; Farber, L. *J. Alloys Compd.* **2002**, *346*, 116.
- (5) Slater, P. R.; Irvine, J. T. S. *Solid State Ionics* **1999**, *120*, 125.
- (6) Slater, P. R.; Irvine, J. T. S. *Solid State Ionics* **1999**, *124*, 61.
- (7) Kaiser, A.; Bradley, J. L.; Slater, P. R.; Irvine, J. T. S. *Solid State Ionics* **2000**, *135*, 519.
- (8) Ikea, T.; Haraguchi, T.; Onodera, Y.; Saito, T. *Jpn. J. Appl. Phys.* **1971**, *10*, 987.
- (9) Kirk, C. A.; Stennett, M. C.; Reaney, I. M.; West, A. R. *J. Mater. Chem.* **2002**, *12*, 2609.
- (10) Miles, G. C.; Stennett, M. C.; Pickthall, D.; Kirk, C. A.; Reaney, I. M.; West, A. R. *Powder Diffraction* **2005**, *20* (1), 43.
- (11) Stennett, M. C.; Miles, G. C.; Sharman, J.; Reaney, I. M.; West, A. R. *J. Eur. Ceram. Soc.* **2005**, *25*, 2471.
- (12) Miles, G. C.; Stennett, M. C.; Reaney, I. M.; West, A. R. *J. Mater. Chem.* **2005**, *15*, 798.
- (13) Levin, I.; Stennett, M. C.; Miles, G. C.; Woodward, D. I.; West, A. R.; Reaney, I. M. *Appl. Phys. Lett.* **2006**, *89*, 122908.
- (14) Kamba, S.; Veljko, S.; Kempa, M.; Savinov, M.; Bovtun, V.; Vanek, P.; Petzelt, J.; Stennett, M. C.; Reaney, I. M.; West, A. R. *J. Eur. Ceram. Soc.* **2005**, *25*, 3069.
- (15) Stennett, M. C.; Reaney, I. M.; Miles, G. C.; West, A. R. *J. Am. Ceram. Soc.* **2007**, *90* (3), 980.
- (16) Stennett, M.; Reaney, I. M.; Miles, G. C.; Woodward, D. I.; West, A. R.; Kirk, C. A.; Levin, I. *J. Appl. Phys.* **2007**, *101*, 104114.
- (17) Zhu, X. L.; Chen, X. M.; Liu, X. Q.; Li, X. G. *J. Appl. Phys.* **2009**, *105*, 124110.
- (18) Prades, M.; Beltrán, H.; Masó, N.; Cordoncillo, E.; West, A. R. *J. Appl. Phys.* **2008**, *104*, 104118.
- (19) Larson, A. C.; Von Dreele, R. B. *General Structure Analysis System (GSAS)*; Los Alamos National Laboratory Report LAUR 86-748; Los Alamos National Laboratory: Los Alamos, NM, 1994. Toby, B. H. *J. Appl. Crystallogr.* **2001**, *34*, 210.
- (20) Zhu, X. L.; Wu, S. Y.; Chen, X. M. *Appl. Phys. Lett.* **2007**, *91*, 162906.
- (21) Zhu, X. L.; Chen, X. M.; Liu, X. Q.; Li, X. G. *J. Mater. Res.* **2008**, *23*, 3112–3121.
- (22) Zhu, X. L.; Bai, Y.; Liu, X. Q.; Chen, X. M. *J. Appl. Phys.* **2011**, *110*, 114101.
- (23) Torres-Pardo, A.; Jiménez, R.; González-Calbet, J. M.; García-González, E. *Inorg. Chem.* **2011**, *50*, 12091.
- (24) Arnold, D. C.; Morrison, F. D. *J. Mater. Chem.* **2009**, *19*, 6485.
- (25) Beltrán, H.; Prades, M.; Masó, N.; Cordoncillo, E.; West, A. R. *J. Am. Ceram. Soc.* **2010**, *93*, 500.
- (26) Prades, M.; Masó, N.; Beltrán, H.; Cordoncillo, E.; West, A. R. *J. Mater. Chem.* **2010**, *20*, 5335.
- (27) Masó, N.; Prades, M.; Beltrán, H.; Cordoncillo, E.; Sinclair, D. C.; West, A. R. *Appl. Phys. Lett.* **2010**, *97*, 062907.
- (28) Beltrán, H.; Prades, M.; Masó, N.; Cordoncillo, E.; West, A. R. *J. Am. Ceram. Soc.* **2011**, *94*, 2951.
- (29) Zhang, Q.-L.; Masó, N.; Liu, Y.; Yang, H.; West, A. R. *J. Mater. Chem.* **2011**, *21*, 12894.
- (30) Prades, M.; Beltrán, H.; Cordoncillo, E.; Alonso, P. J.; Masó, N.; West, A. R. *Phys. Status Solidi A* **2012**, *209* (11), 2267–2272.